Development of a Capacitive Sensor for In-Pile Materials Monitoring

A Thesis Presented for the

Master of Science

Degree

The University of Tennessee, Knoxville

Tyler M. Naughton

May 2020

Dedication...

To my parents, you both have showered me with enough support, guidance, and love to last several lifetimes.

And to Dr. Jamie Coble, for providing me with wonderful experience. If not for her leadership and patience then this project would not where it is today.

Acknowledgments

This work is funded by the University of Tennessee's Science Alliance Joint Directed Research Development program; a collaboration with Oak Ridge National Laboratory. The author would like to acknowledge assistance from: Mr. Mike Curic for EMS assistance, Ms. Ashly Pearson and Mr. Scott Emert for sensor fabrication assistance, and Mr. Phillip Scruggs and Dr. Xueping Li for assistance in printing the sensor casing.

Abstract

The nuclear power industry is taking further advancements in the development and testing of advanced fuel compositions, such as accident tolerant fuel. Long-term performance of these newly developed fuels is estimated through physics-based simulation models of irradiation-, temperature-, pressure-, etc.-induced material degradation. model predictions are validated with the measurement and characterization of fuel pin evolution. Linear voltage differential transformers (LVDT) are commonly used to measure fuel pin evolution parameters. However, due to the bulky size and direct touch, LDVTs are often precluded from being used in high performance research reactors. There is crucial need to develop a sensor that can provide real-time reliable and robust material evolution measurements in a highly irradiated environment. A capacitance-based displacement sensor was then simulated and developed at the University of Tennessee to provide a direct measurement of in-pile dimensional change during irradiation. Capacitance-based sensors have been previously investigated for axial dimensional changes in a highly irradiated environments, and have been suggested that such sensors may provide reliable in-pile measurements. Simulated capacitance responses of various creep tube diameters were constructed with simple finite element method models (FEMM), which generate a meshed region over a two-dimensional environment. Due to the simple geometries, it was assumed that the mean capacitance value from the FEMM models were equal to that of a three-dimensional system. Following the simulated models, an Analog Devices 7747 evaluation board was used to provide real-time evaluation of various creep tubes. Diameters of tested/simulated creep tubes were increased by small increments (0.127 millimeter or 0.0254 millimeter) to determine if small dimensional differences could be easily differentiated. Both simulated and experimental capacitance trends showed that capacitance values could easily be distinguished from one another, indicating that the proposed sensor model could provide robust measurements. Troubleshooting in the development of experiment, sensor, and simulated along with potential areas for future research and development are discussed.

Table of Contents

List of Tables

List of Figures

Chapter 1

Introduction

Advanced fuel compositions are an active field of development in the nuclear power industry. Long-term prediction and evaluation of these fuel compositions are estimated with physics-based simulations of irradiation-, temperature-, and pressure-induced material property evolution (such as creep and swelling). As these fuels are deployed in test reactors, measurement and characterization of the fuel pin evolution is used to validate prediction models. Commonly a pressurized creep tube is used to measure the irradiation creep, which can be small as a few microns. The irradiation creep depends on the tube's material of interest, the applied hoop stress, the irradiation dose, and the initial diameter of the creep tube. However, irradiated creep measurements are rather challenging to measure during the test reactor's operation. Currently available sensors have a limited operational range and accuracy within the test reactor environment. These limited operational ranges cause for diameter alterations to be measured primarily after irradiation resulting in only displacement measurements for a singular time/dose, instead of during the entire operational cycle. An advanced sensor that can provide real-time dimensional measurements during reactor operational time is thus needed.

Commonly such evolution parameters are measured utilizing a linear voltage differential transformer (LVDT) due to their high accuracy and near infinite resolution within noisy environments. However, LDVTs by design are sensitive to external magnetic fields and temperature fluctuations [2]. An external magnetic field will alter the voltage signal on the sensor. An altered voltage signal influences the generated current and magnetic field, which will then cause for either an decrease or increase of the measured output signal [21]. Influence from external magnetic fields can be reduced by applying additional components in the sensor's circuitry and/or addition of a shield around and inside the sensor. But with these additions, the LDVTs increase in size and cost. With the alterations, the LDVT is still heavily impacted by the high temperature changes within the reactor, causing LDVTS to have a lower limited operational range (350-500 °C). Because of the high power density, operational temperatures, and small sizes of test reactors, accelerated materials irradiation studies generally precludes the use of LVDTs in these reactors. There is a critical need for sensors that provide real-time data regarding material evolution under highly accelerated irradiation. These sensors would ideally have a small profile and the ability to withstand irradiation at extremely high dose rates and temperatures for extended periods of time.

Capacitance-based sensors have been proposed and initial concepts demonstrated for axial dimensional change during irradiation experiments [13], suggesting this measurement approach may be robust to high radiation environments. One such example is with the application of a fixed gas pressure on a mechanical bellows, that would then apply mechanical loading onto a stack of fuel specimens [13]. This experimental setup is placed with a triple containment within a three gas-filled tube of a high flux reactor's (HFR) tube, as shown in Figure 1.1. This sensor set-up measures the real-time displacement of the material sample between the two capacitor plates.

Capacitor electrodes were placed at the top and bottom of the fuel stack, with samples kept at the center of the two capacitive electrodes. Direct contact between the electrodes and fuel stacks are done so as to quantify dimensional changes with the fuel stack. Each tube holds three samples at various heights (lower, middle, and upper) providing large data sets. During the reactor's operational cycle, the material samples would experience some dimensional change from irradiation. Sample dimension changes are measured and recorded as capacitance signals. As the distance between the capacitor plates alters, so does the capacitance signal. With the applied fixed pressure from the insulated gas, the changes in capacitance signals can be measured with high accuracy. With the inclusion of multiple capacitance electrodes, displacement measurements may be independently monitored.

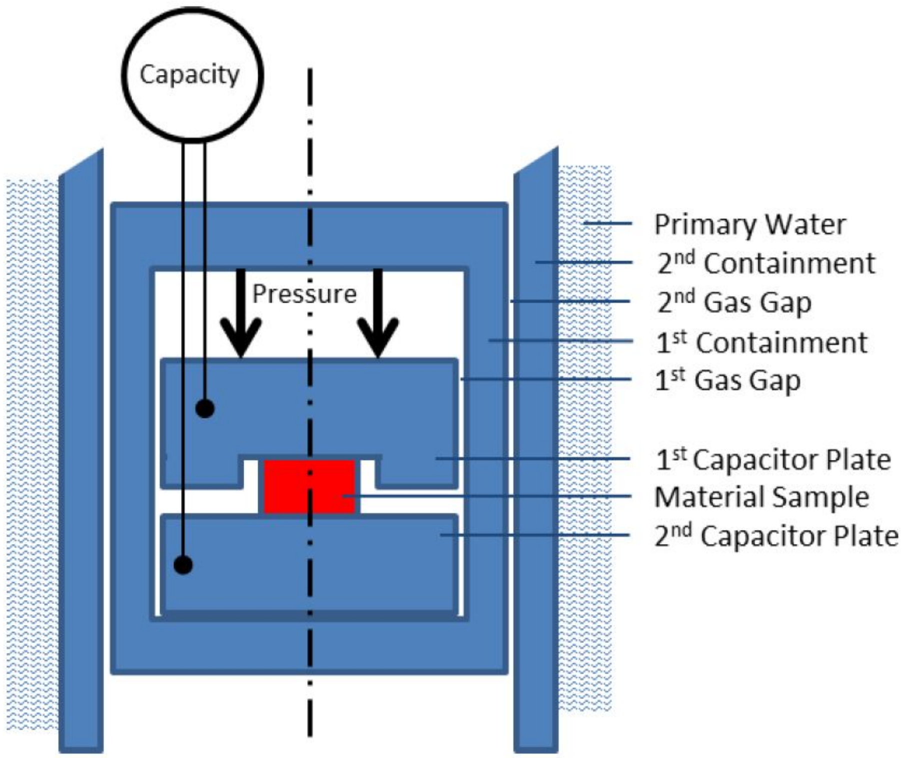

Figure 1.1: Capacitance-based sensor within HFR TRIO tube. [13]

Small gaps are located between the tube's containment layers, which allow for testing under the facility's high temperature range. Alteration of the gas mixture composition (neon, helium, and nitrogen) in each gap allows for local temperature control. As the composition of the gas alters so too does the thermal conduction of the gas mixture. The center-most samples will need the highest operational range (900 to 1250 °C) because of the high nuclear heating in the region. This may be achieved by placing more conductive gases (e.g. Helium) than insulating gases (e.g. Argon). If the external temperature exceeds this range, then the insulating material and cables would experience expansions that vary based on the thermal expansion of each material. For non-cable materials, this can cause an increase in the capacitance noise and drift. Cables would experience a connection failure before the highest temperature range (1300 °C) causing for a signal loss. If excessive pressure is placed onto the fuel sample, then sample portions may crack or break off. In these scenarios the displacement/capacitance terms will be given complex nonlinear additions. Because of these nonlinear additions, a non-direct contact should be considered for capacitance-based sensors.

Non-direct capacitance-based sensors measure displacement through the relative, non-parallel movement of a suspended electrode and a fixed electrode [26, 19]. For this research, the fixed electrode is a ring sensor surrounding the pressurized creep tube while the pressurized creep tube itself serves as the suspended electrode, shown in Figure 1.2. A similar sensor was developed by Idaho National Lab with their impedance-based diameter gauge [4]. This gauge design allows for larger control of electrode displacement because the outer electrode is able to placed at user defined locations with the use of a gear system. The capacitance of the general system can be found as:

$$C = \frac{2\pi\epsilon L}{cosh^{-1}(\frac{r^2+R^2-\delta^2}{2rR})} \tag{1.1}$$

where ϵ is the absolute permittivity, L is the length of the cylinders, r is the outer radius of the inner cylinder (cladding), R is the radius of the outer cylinder (sensor), and δ is the distance between the centers of the sensor and rod. Equation 1.1 assumes that the electrodes are part of a simple resistor capacitor (RC) parallel circuit and that no parasitic effects are present.

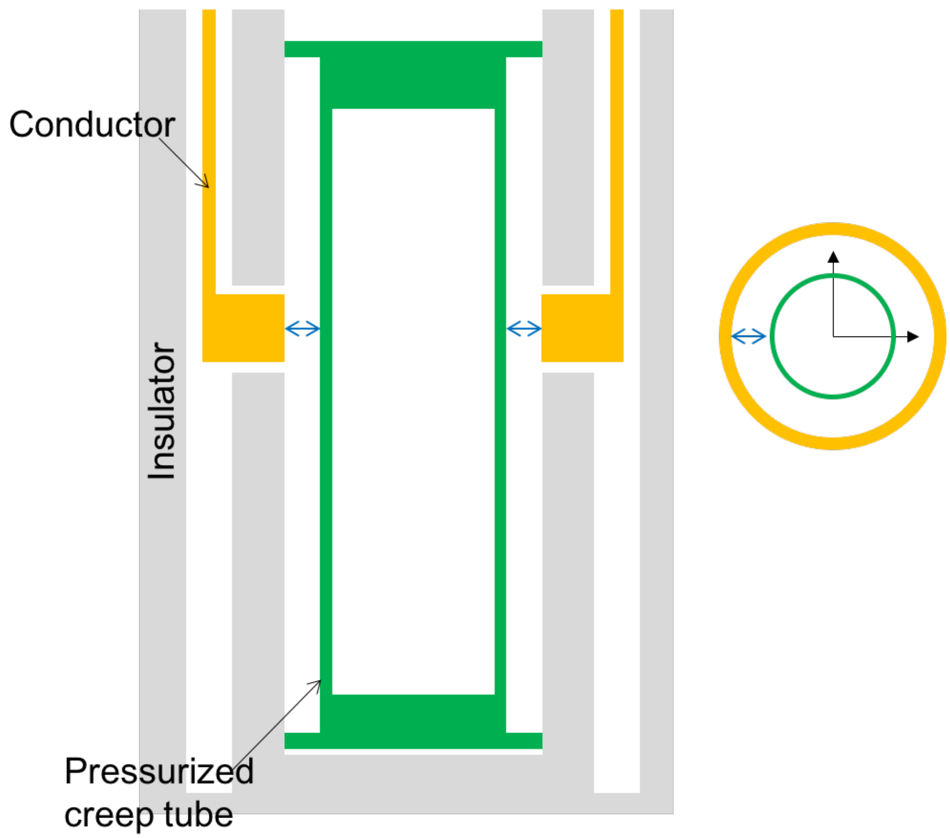

Figure 1.2: Capacitance-based radial dimensional change sensor design

If there is no offset between the two centers, then equation 1.1 becomes concentric and simplifies to:

$$C = \frac{2\pi\epsilon L}{ln(\frac{R}{r})}. \tag{1.2}$$

For this work, the concentric model will be heavily used to extend the concept to radial measurement. This thesis presents initial design, simulation, and testing of a capacitive dimensional change sensor. Chapter 2 discusses the the theory behind capacitance and capacitance displacement sensors while also looking at other displacement sensor types. Finite element method modeling (FEMM) theory and simulated models are present in chapter 3; the experiment setup and initial holding systems are shown in chapter 4. Simulated and measured capacitance results from various sized copper creep tubes are shown within chapter 5. Chapter 5 also discusses the troubleshooting methods and best practices used in the experimental measurements. Lastly, a summarized conclusion of this work is given in chapter 6.

Chapter 2

Background

2.1 Capacitance Theory

In an environment with N possible electrodes, such as in Figure 2.1, the capacitance value is shown as the quotient of induced charge and potential voltage difference, shown in Equation 2.1. This equation theoretically indicates that selected electrodes should not be influenced by neighboring electrodes. However, in practice neighboring electrodes may have some influence on the capacitance signal if the capacitor is not properly shielded. This will be discussed in further detail later on. However, Maxwell originally shielded the electrodes with a guard ring. This ring is designed to be much larger than the electrodes, and give the fixed electrode the same voltage potential as the suspended electrodes, resulting in a homogeneous electric field around the electrodes that allows for an easier method of measuring only the polarity movements between the electrodes. However, this method is still susceptible to interference from higher electrical fields outside the system.

$$Capacitance\,(C) = \frac{Charge(Q)}{Voltage\,(V)} \tag{2.1}$$

Capacitors are able to store an electrical charge over two plates. Basic capacitor types are two parallel plates separated by some insulated material, shown in Figure 2.2. The insulating material is commonly refereed to as the dielectric, and will block DC currents from flowing

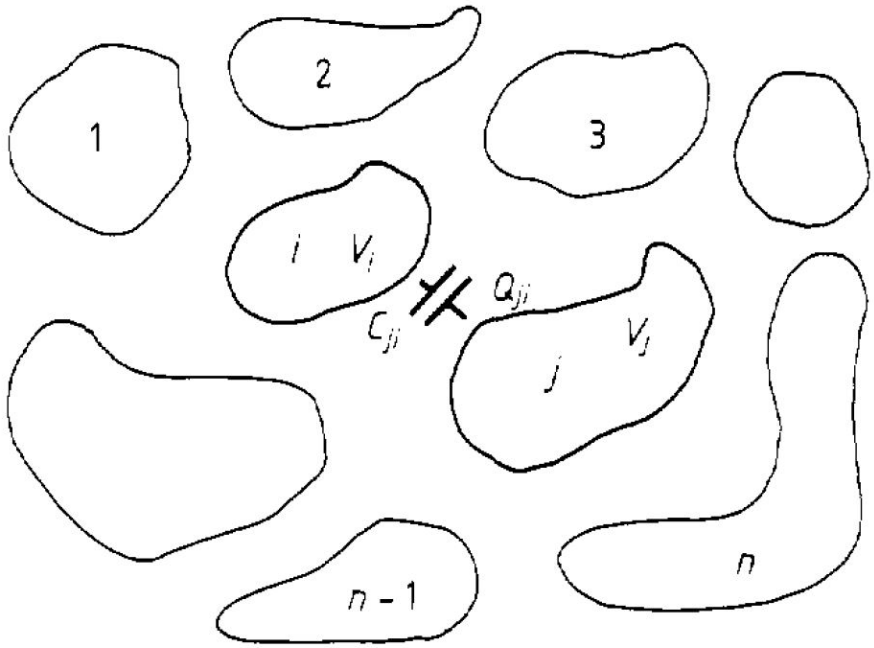

Figure 2.1: Example of parallel plate capacitor within a large electrode environment. [7]

through the capacitor. Instead of a DC current, the conductive plates have an alternating charge placed onto them, induced by the voltage terms on each plate.

Collective charges are equal on each plate, but have a different polarity (either positive or negative) depending on the incoming voltage signal. When an alternating current (AC) is place onto the capacitor, the polarities will begin to move between the plates. Polarity movement will result in a current signal (i) between the plates. This signal is proportional to the capacitance between the plates, as shown in Equation 2.2:

$$i = \frac{dq}{dt} = \frac{d}{dt} * \left(\frac{\epsilon * Plate\,Surface\,Area}{distance}\right) * v = \frac{\epsilon * Plate\,Surface\,Area}{distance} * \left(\frac{dv}{dt}\right) = C * \left(\frac{dv}{dt}\right) \tag{2.2}$$

where ϵ is the dielectric constant of the medium between the plates. From this equation, a simple parallel plate capacitance is given as:

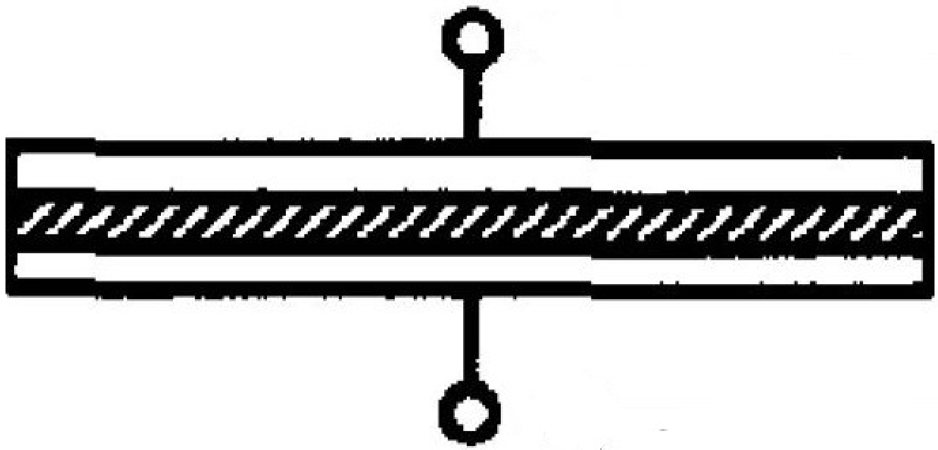

Figure 2.2: Example of parallel plate setup. Conductive surfaces are separated by some dielectric material [18]

$$Capacitance = \frac{\epsilon * Plate\,Surface\,Area}{Plate\,Distance} \tag{2.3}$$

Equation 2.3 can be altered for more complex geometries and medium combinations. However, with more complex scenarios comes the possible addition of nonlinear terms. For example, a cylindrical capacitor's conductor plates are arranged with one overlapping another. If the inner rod, is not placed within the center of the outer ring, then the distance between each rod is non-uniform. This causes sections of the capacitor to have a larger current signal due to faster polarity movement. A displacement approximation can be made by dividing the outer electrode into an even number of sections, as shown in Figure 2.3. Such approximations look at the capacitance values from each capacitance electrode.

Figure 2.3 depicts an inner electrode that is centered to the outer sections. Based on the capacitance signals from each electrode section, the displacement values can be found for the x and y axis. For these values, it assumes adds all positive quadrant values and removes all negative values, as shown in Equation 2.4. For example if all sectors have the

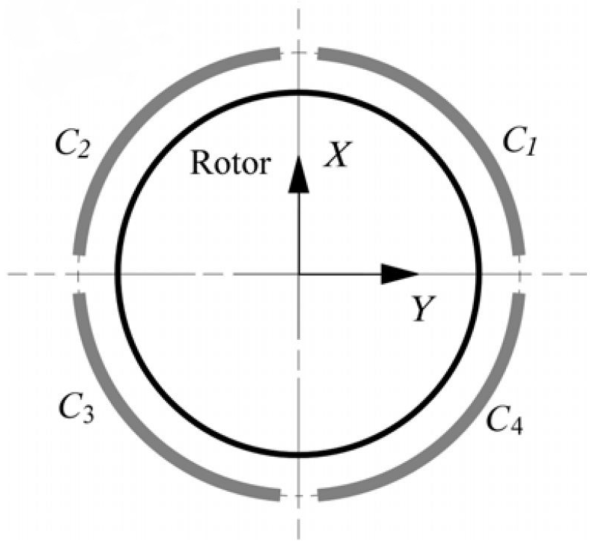

Figure 2.3: Cylindrical sensor with outer electrode divided into four equal sections. Inner electrode is an equal distance to all outer sections. [11]

same capacitance value, then it will indicate zero-value displacement values. This means that either no displacement has occurred in the system or that all sections saw an equal amount of displacement, but it is rare for all sectors to experience an equal displacement value so it is typically assumed to indicate no displacement.

$$\begin{aligned} X_{cap} &= (C_1 + C_4 - C_2 - C_3) \\ Y_{cap} &= (C_1 + C_2 - C_3 - C_4) \end{aligned} \tag{2.4}$$

For systems where the inner rod is not centered, these equations give poor approximations. For example if the rod is placed closest to electrode 1 (C_1) then the capacitance value will be larger by default, resulting in an improper displacement value. In addition, the capacitance from electrode 4 (C_4) will not be equal for the entire electrode. Because of this, an average capacitance value will most likely be taken, but this value will be heavily influence by the distance to the inner electrode. These distances will place improper weight on the mean value. For a better capacitance approximation, the angles and displacement from all electrodes should be considered. These values can be shown in Figure 2.4. Considering these terms, the capacitance values are:

$$
\begin{aligned}
X &= \frac{\epsilon bw}{\delta}\frac{2}{\sqrt{1-(\frac{\alpha^2}{\delta^2})}}arctan\frac{2\frac{\alpha}{\delta}\sqrt{1-(\frac{\alpha^2}{\delta^2})}sin\zeta cos\beta}{1-\frac{\alpha^2}{\delta^2}(sin^2\zeta+cos^2\beta)} \\
Y &= \frac{\epsilon bw}{\delta}\frac{2}{\sqrt{1-(\frac{\alpha^2}{\delta^2})}}arctan\frac{2\frac{\alpha}{\delta}\sqrt{1-(\frac{\alpha^2}{\delta^2})}sin\zeta sin\beta}{1-\frac{\alpha^2}{\delta^2}(sin^2\zeta+sin^2\beta)}.
\end{aligned}
\tag{2.5}
$$

Derivation of these equations are shown in [11]. This approximation considers the displacement between multiple electrodes; however, it does not account for any external disturbances that may occur during testing. Discussion of these disturbances will occur in greater detail later on.

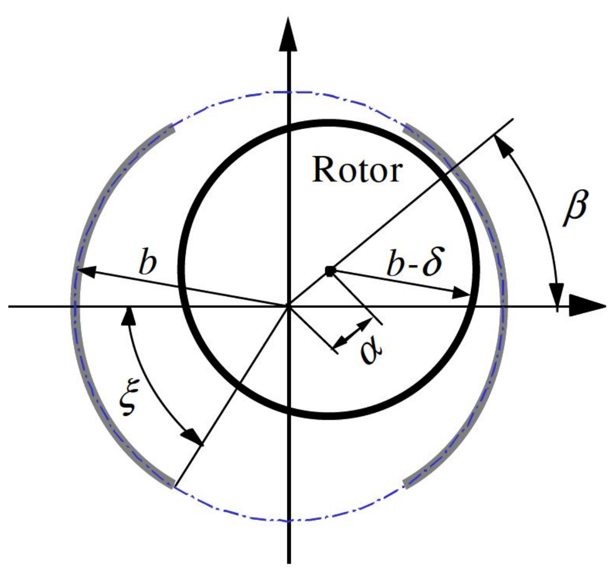

Figure 2.4: Cylindrical sensor with inner electrode at an uneven distance between outer electrode sections. [11]

2.2 Linear Voltage-Differential Transformers

Various devices and methods are used to measure a system's displacement reading. Linear voltage-differential transformers (LVDTs) are commonly used displacement sensors for in-pile applications. LVDTs are typically used to measure the linear displacement along a single axis. Typically an LVDT is composed of seven main components: primary coil, two secondary coils, ferromagnetic core, tube, shield, and shaft. Figure 2.5 depicts an average LDVT; however, the primary and secondary regions in the figures are coils. Coil windings are such that the primary and secondary coils are spun in different directions. The secondary coils are typically placed at the end of the primary to give a series-opposing circuit. Series-opposing circuits means that the coils are connected in series, but in different directions resulting in the input and output signals of the secondary coils to be out of phase and causing the output signal to be a measure of the displacement's direction (phase) and distance (amplitude).

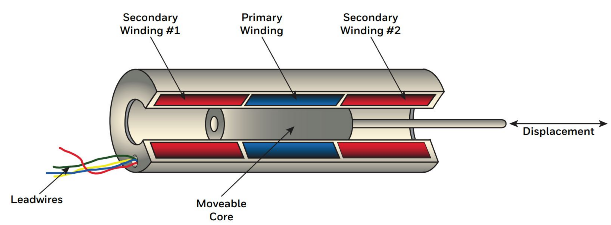

Figure 2.5: Example of linear voltage differential transformer. [10]

The core is large enough to couple the primary and secondary coils. This allows for the magnetic field generated in the primary coil to be influenced by the secondary regions. Coupling between the secondary coils can determine the displacement signal's amplitude and direction. When the core is perfectly placed in the center of both secondary coils, then the voltage from each signal is equal and will cancel out. However, as the core is moved by displacement, one coil will have a larger signal than the other, resulting in an offset signal that is proportional to the displacement's direction and distance [12].

Advantages of the LDVT's design allows for the sensing core to have theoretically no wear, because the rod is made of a ferromagnetic material and placed in the center of all coils. During operation, the electromagnetic fields of both coils allows for the core to float freely. By floating freely, the core region is susceptible to displacement changes. However, the core region may have difficulty moving due to the operational temperature. If the LDVT is placed in a high temperature environment, then the core material may experience an expansion. Differences in expansion of core materials can lead to zero-shift error and changes in the starting/calibrated value. Along with expansion probabilities, if the operating temperature alters enough, then the coil material (typically a copper alloy) may experience a change in coil resistance. Resistance changes can alter the coil impedance values. If the impedance value increases, then the coils may experience a current drop. Significant current drops lead to scaling errors in the output and sensitivity levels. There are possibilities to curb temperature effects such as use of manganin wires in the winding or inclusion of a constant-current power source, external resistor, and/or thermistor in the primary and secondary circuist [22]. However, these additions will increase the cost of the devices and make it potentially more bulky. If the device becomes larger in size, then it may have issues with fitting in select environments. But most important is that these additions may not be beneficial if there is a vast temperature increase between the calibration temperature and operating temperature. Because of this, LDVTs should be used in regions with small operational temperatures.

2.3 Capacitance Displacement Sensors

Due to the disadvantages and limitations of existing sensors, a new sensor type is needed to verify displacement and swelling of a test reactor's fuel pin. A proposed alternative is with the capacitance-based displacement sensor type. Capacitance-based sensors have been proposed and initial concepts demonstrated for axial dimensional change during irradiation experiments [13], suggesting this measurement approach may be robust to high radiation environments. In addition these sensor types have a reduced size, due to utilizing the fuel pin as the suspended electrode.

Capacitance based sensors measure the displacement through relative, nonparallel movement between a fixed and suspended electrode. When a fixed voltage is supplied to the conductive electrodes, then an electromagnetic field is generated. Opposing polarities are formed on each of the electrodes. An alternating voltage source causes for polarities to move between the electrode, resulting in a alternating current signal; this signal is proportional to the capacitance between the two electrodes. The surface area and proximity of the two electrodes determines the capacitance and current signals between the objects. Distance between the electrodes and capacitance signal shows to have an inverse relationship. As the distance decreases, the opposing polarities have a smaller distance to move, allowing them to move at a faster rate. With a faster polarity movement rate, the current and capacitance signal will increase.

For this research, a capacitance-based displacement sensor is developed as a fixed ring around a suspended creep tube. The suspended creep tube serves as the suspended electrode while the sensor ring serves as a fixed electrode, as shown in Figure 1.2. Physical models used to find the capacitance between the electrodes are derived in [9]. Capacitance per unit length ($\frac{C}{L}$) approximations for cylindrical electrodes are shown as:

$$\frac{C}{L} = \frac{2\pi\varepsilon_r\varepsilon_0}{ln\left(\frac{r_o}{r_i}\right)} \tag{2.6}$$

where ε_0 is the permittivity of free space, ε_r is the relative dielectric permittivity, r_i is the radius of the inner conductor (the outer radius of the creep tube), and r_o is the radius of the outer conductor (the inner radius of the sensor). For this research, it is assumed that the sensor's inner radius remains fixed and that only the creep tube will experience dimensional changes. As discussed previously, if the inner radius is placed at a skewed distance, then the capacitance signal will be exposed to improper weights; for this work, the two electrodes are assumed to remain concentric. Relationships between the electrodes can be shown using a finite element analysis, shown later on within the various simulation methods.

Capacitance displacement sensors will need to be properly shielded. If the sensor is not properly shielded then the generated capacitance signals will be exposed to interference from external noise terms (e.g. magnetic fields, coupling, etc.). The shield acts as Gaussian equipotential surface that will terminate electrical fields by rerouting them back to a grounded signal without affecting the internal components. However, a shield will only work if the capacitance circuit's ground path has a low impedance signal. Higher impedance paths will result in a floating shield, which provides no protection against interfering signals. Noise dominates at higher impedance because of the following relationship:

$$Noise = Current\,(i) * Impedance\,(Z). \tag{2.7}$$

Because of the high impedance values, the capacitor circuit will have a low interference loop [25]. A low interference loop means that instead of being grounded, the loop has some potential difference. This difference is typically caused by multiple paths to a singular grounded signal, resulting in a closed loop that is highly susceptible to external magnetic fields. This can be solved by either breaking the loop in the circuit or switching the impedance terms.

The following chapters describe the simulation and experimental validation of the proposed capacitance-based sensor design. Chapter 3 discusses the sensor design and approach to simulation. The experimental set-up and construction is detailed in Chapter 4. Chapter 5 presents results of both simulation and laboratory measurements.

Chapter 3

Simulations

There are many methods and techniques available for simulating capacitance values for various sensors. When simulating a capacitance sensor, most techniques first assume that the sensor is composed of two parallel plates. With this assumption, it is believed that the plates are perfectly smoothed and aligned properly. If there is a deviation on the plate, then there can be a significant impact on the capacitance signal [16]. A growth in a plate will cause for a larger capacitance signal, and an improper alignment will reduce the impacted surface area, thus giving a smaller capacitance signal. Another issue with these simpler plates comes from the amount of medium layers and layer thicknesses. A single medium layer's capacitance per unit signal is proportional to the medium permittivity (ϵ):

$$C' = g' * \epsilon \tag{3.1}$$

where g' is the proportionality coefficient. Plates comprised of more than one medium causes for Equation 3.1 to take on complex terms (one for each layer). Derivation of these complex terms are shown in [1]. For example, a two layer medium's (Figure 3.1) capacitance per unit length signal is:

$$\frac{1}{C'} = \frac{2}{(\epsilon_1 + \epsilon_2)g'_{13}} + \frac{(\epsilon_1 - \epsilon_2)}{(\epsilon_1 + \epsilon_2)}(\frac{1}{\epsilon_2 g'_{23}} - \frac{1}{\epsilon_1 g'_{12}}) \tag{3.2}$$

where g'_{23} is the line proportionality between electrodes, g'_{12} is the line proportionality between electrode's shields, and g'_{13} is the line proportionality when $\epsilon_1 = \epsilon_2$.

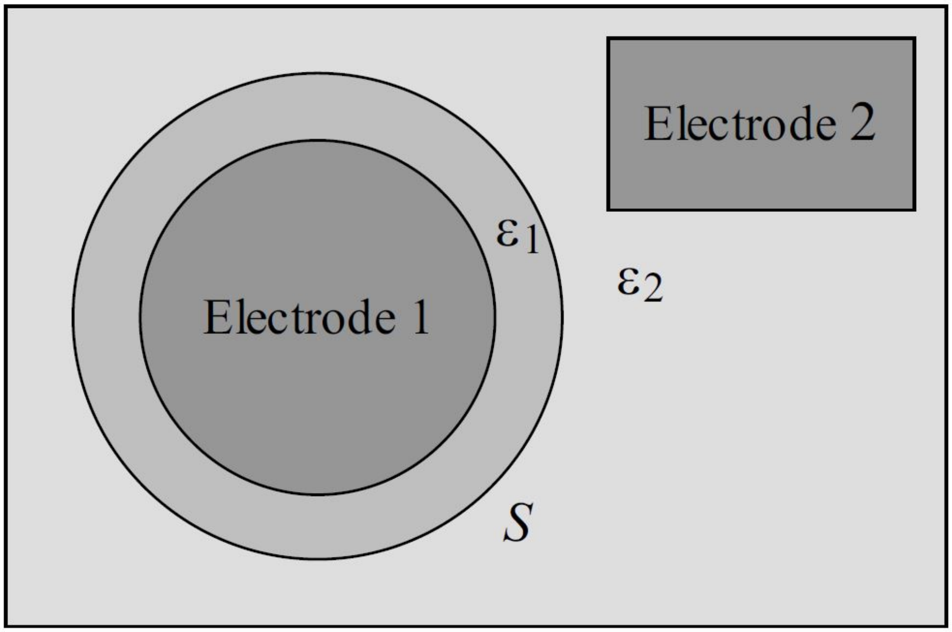

Figure 3.1: Capacitance sensor with two medium layer. Each electrode is within a differeing medium. Electrodes are shielded from one another and outside effects with shielded surface (S). [1]

More complex capacitance geometries are derived by Queiroz in [20]. For an empty cylindrical sensor, the electrodes are two opposing sections. It is assumed that the two sections are exactly opposite and rectangular in shape. This allows for no deviations in alignment and provides a simple comparison to parallel plates. With these assumptions, the cylindrical capacitance signal (similar to **??**) is:

$$C = \frac{\varepsilon_0 \varepsilon_r l}{\pi} ln \left(\frac{sin[0.5(\varphi_1 - \varphi_3)] * sin[0.5(\varphi_2 - \varphi_4)]}{sin[0.5(\varphi_2 - \varphi_3)] * sin[0.5(\varphi_1 - \varphi_4)]} \right) \tag{3.3}$$

where φ_1, φ_2, φ_3, and φ_4 are all the angles to an electrode side. Equation 3.3 utilizes the length of the entire rod. A more detailed form of these variables are shown in Figure 3.2.

For a non-hollow sensor, Equation 3.3 can be applied. However, this equation assumes that the rod is perfectly centered. Non-centered rods results in differing distances and

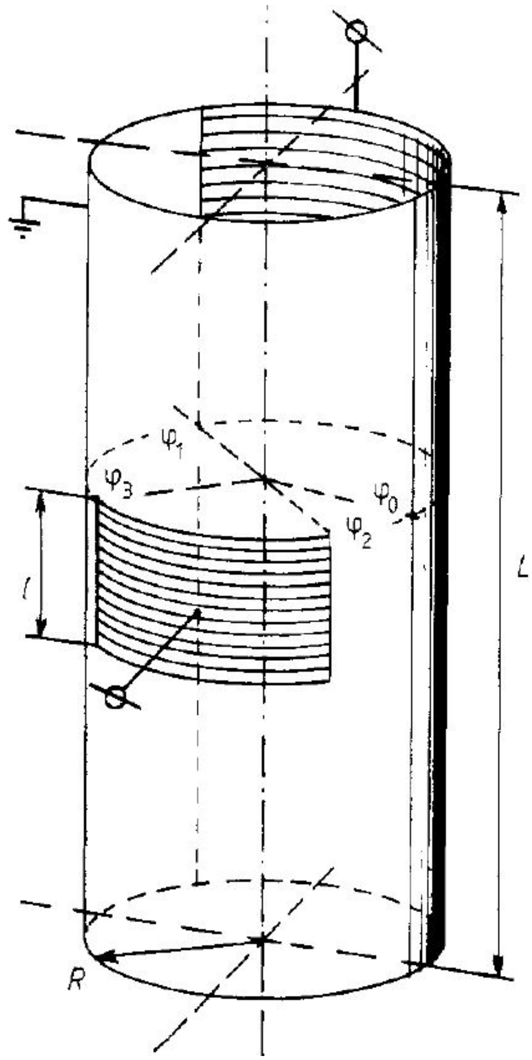

Figure 3.2: Hollow capacitance sensor with assumed rectangular electrode sections. ε_0 and ε_1 reference the angles to one electrode section sides and ε_2 and ε_3 to the other electrode section's side. [8]

misalignment between the two electrodes. This misalignment causes for varying capacitance signals, which can potentially cause for signal drift issues. Smaller distance sections will have a larger capacitance signal than the sections with larger distances [5], because opposing polarities will have less distance to move between the closer sections allowing for a larger current or capacitance signal. This research will assume that all inner electrodes are placed at the center of the outer electrode, giving each segment an equal distance and capacitance signal.

Simulations were done in order to understand how rod swelling impacted capacitance signals. Two programs were used to record simulated values. The first program is an add on to AutoCad Inventor called ElectroMagnetic Simulation (EMS). EMS works by taking user developed volumes, as shown in Figure 3.3, and placing either fixed or floating voltage signals onto them.

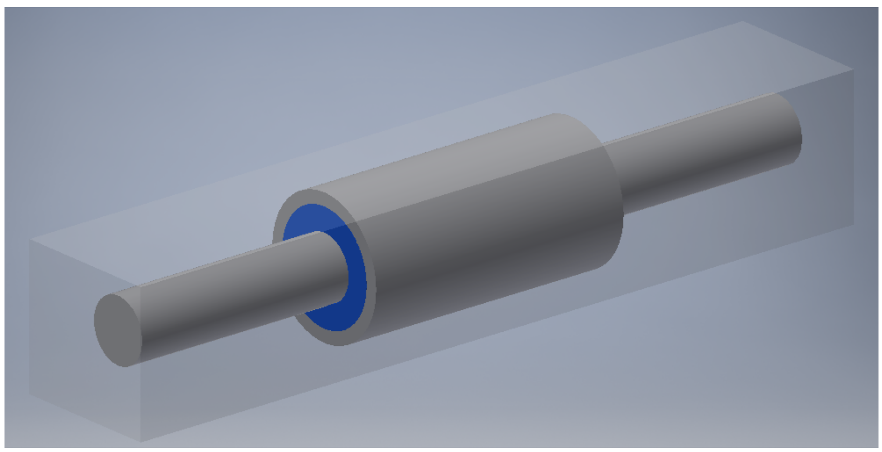

Figure 3.3: Example of volumes used in EMS simulation.

Signal placement helps define boundary conditions and regions of interest. EMS determines the regions of interest for the capacitance signal with a finite element method technique. A finite element technique breaks the region of interest into user defined blocks or mesh. Each defined block section has a preset number of equations. These equations utilize boundary conditions and the outputs from other blocks to solve the block's charge density using Green's function, derived in [23]. When all equations are solved in an individual block, the equations' output values are sent to neighboring blocks to be used as inputs. This process continues until all blocks are solved and a mean capacitance value is sent to the user. However, a larger number of blocks are required to ensure an accurate value. Using more blocks increases the computational time and power needed to solve the preset equations. Because of this, the EMS program had limited use for simulating capacitance trends. Despite this, the author would like to thank those at EMWorks for their assistance with EMS.

3.1 FEMM

Finite element method modeling (FEMM) is used in a variety of applications ranging from position sensors to high speed motors. This simulation technique works as a solver for two-dimensional and/or axisymmetric electrostatics and low frequency magnetic problems [14]. Prior to FEM modeling, it was difficult to predict the displacement (and therefore capacitance) between two active electrodes, because the electromagnetic field between the electrodes will be affected by interfering signals. Most of theses signals are produced from either electromagnetic coupling within the system or external signals. To limit these trends, it is assumed that all materials are perfectly shielded. Assumptions such as these allow individuals to determine an approximate capacitance signal for complex electrode geometries. However, these approximations are limited to cases were the electric field between electrodes is homogeneous [17].

For this research, the FEMM models were developed with a MATLAB script [15]. To develop a volume of interest, a user first determines select edge points for the object. Typically these points are the edges and corners of the interested volume. After all points are placed, volumes are created by connecting the points with select line segments. For the models developed here, these volumes are cut in half. The resulting plane is rotated around the left edge, making a three dimensional object. Defining of materials can be done in the volumes by placing a material node/block label. In these nodes, the materials may be selected from the included library. If the material is not included in the library, then they may be added by defining the material's permittivity in the x- and y- direction and the volume charge density. Used materials from the library include air and copper. In this paper the only material added was polylactic acid plastic (PLA) with permittivity values of 2.7 and a volume charge density of 0 C/m^3. PLA is utilized as the material for the printed holding device, described in the next chapter. Voltage signals or total charges can be then be placed onto the select material regions. For this paper, a $1\,V$ signal is placed onto the copper sensor bar. The copper creep tube rod is given a signal of $0\,V$. The remaining volumes are assumed to have a placed signal of zero volts. When all materials and voltages are placed onto the volumes, a simulated triangular mesh (element size of 0.0025mm) can be placed onto the system.

In creating the simulated mesh, the volumes are broken into smaller triangular regions. Each region will then have a set of equations used to solve for the mean capacitance value within itself. Equations are solved in a similar method as EMS; however, the boundary conditions are slightly different. Instead of being interested in the mean capacitance of one region, FEMM is interested in the mean value from all regions. Mean capacitance values are solved similarly to that of EMS; however, the individual values may either be stored within a $1 \times n$ matrix or given as the mean of every element. Either method will give a slightly higher mean capacitance value than EMS, yet the region in between the sensor and creep tube have the most influence, shown in Figure 3.4. The FEMM simulation gives a mean capacitance value with and without fringing effects. Fringing effects occur when the electrical field between the electrodes extends outward to a wider region [24]. With and without these regions, the results will take roughly 1 minute to create and solve each mesh element. This computational time is much faster than the EMS counterpart.

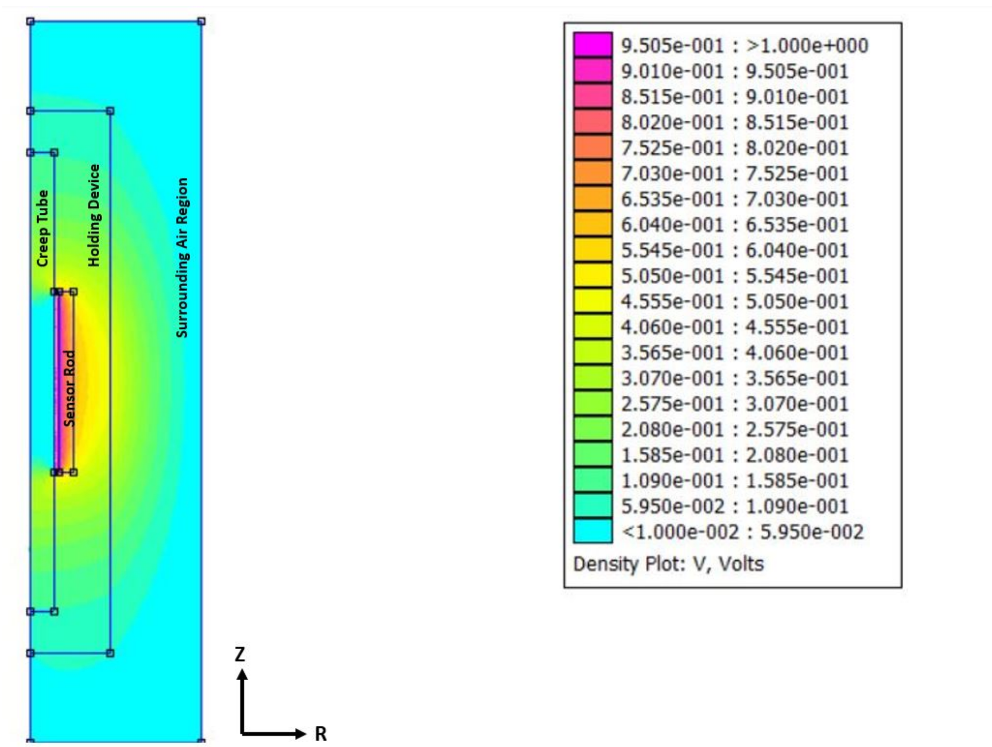

Figure 3.4: Example of two dimensional FEMM reading .Only voltage source is from the copper sensor rod (magenta) with 1 volt. Light blue depecits the lowest voltage signal of zero volts.

Chapter 4

Experiment and Sensor Fabrication

4.1 Experiment Setup

Setup of this experiment is shown in Figure 4.1. To measure the capacitance signals from the sensor rod, an Analog Device 7747 chip and evaluation board were used. This chip is designed to measure signals from either single-ended or differential capacitive sensors with one grounded plate [3]. The current design uses a single-ended capacitance with the creep tube grounded and a potential applied to the sensor. Creep tubes are grounded with an alligator clip that sends a grounded signal from the evaluation board. This clip also ensures that the creep tube is kept stationary during testing; this will be discussed in more detail in the holding device section. The grounded and active signals are sent to the sensor and creep tubes via a subminiature version B (SMB) coaxial cable.

An aluminum enclosure covers the evaluation board. This enclosure shields the evaluation board from external electromagnetic fields and other noise producing signals.

4.2 Holding Device

A holding device was fabricated to ensure that the electrodes were kept stationary and at a fixed distance range between them. If the inner creep tube was allowed to move freely during testing, then it would cause for one section of the sensor to have a disproportionally higher signal due to the a smaller electrode distance in that region. The holder is composed

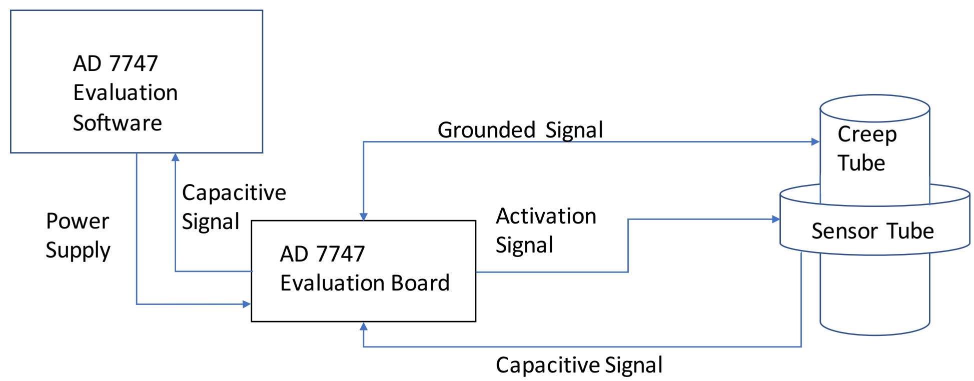

Figure 4.1: Experimental setup for initial sensor measurements

of two parts, a top and bottom, to ensure the electrodes are concentric. The bottom portion of the holder, shown in Figures 4.2 and 4.3, places the creep tube in the center of the holder part. A shelf region is placed around the center of this hole region, that holds the sensor at a fixed location. A smaller solid block is attached to the bottom holder to act as balance for the system. To allow for testing of various sized creep tubes, the hole region is 5.33 mm in diameter. Because of this size, some of the smaller rods (5.08mm and 5.10 mm) are able to move during testing. The top portion (4.4) of the holder was created to limit this free movement. At the center of the holder top is a hole with the same diameter as the holder bottom. When placed on the bottom holder portion, the smaller rods have a reduced amount of space to move in. To further limit this movement, an alligator clip is connected to the rod. With this clip, the creep tube and sensor are kept at a fixed distance from each other during the testing duration. Lastly, the dimensions for both sections are shown in Figure 4.5.

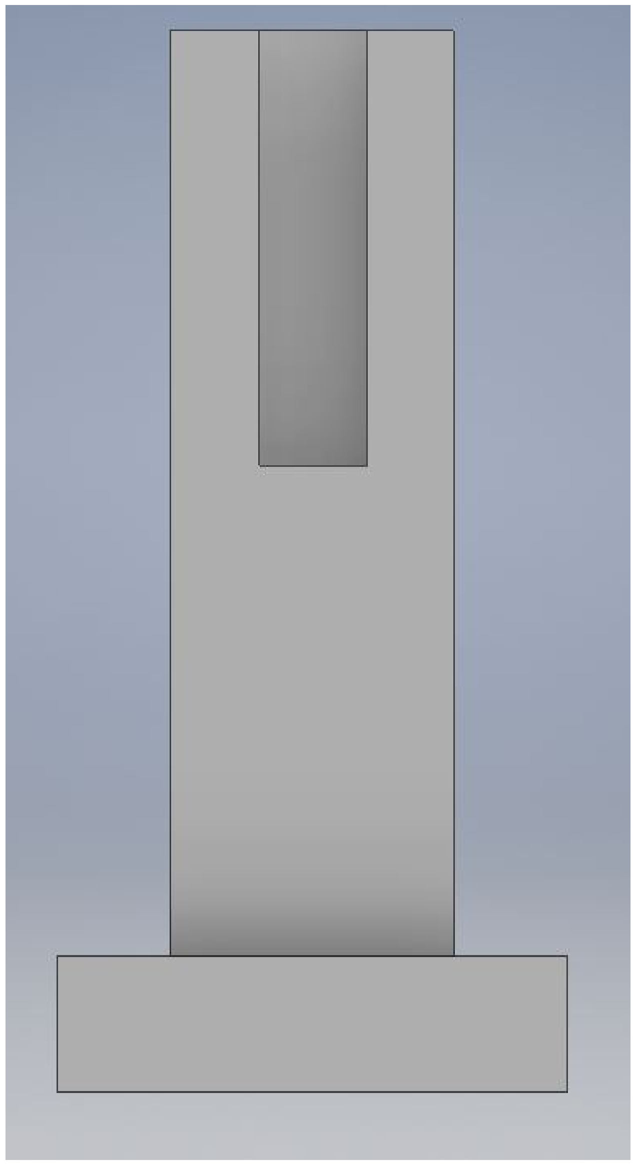

Figure 4.2: Side view of printed holder system's bottom section. The larger section provides weight to the system and prevents tipping during testing processes.

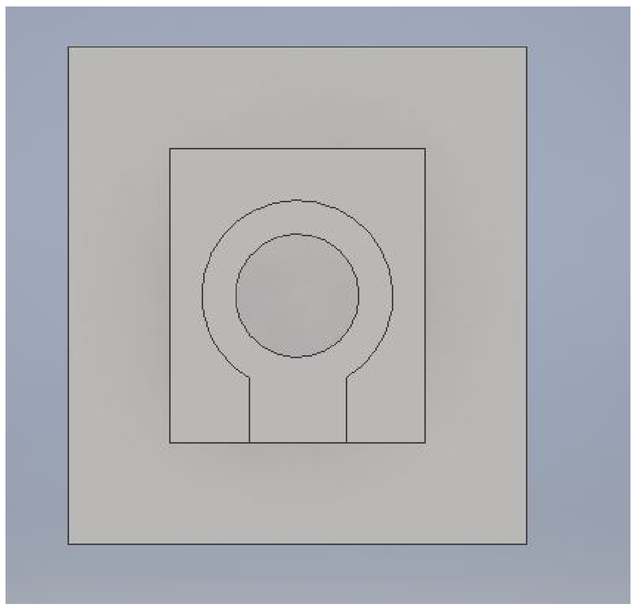

Figure 4.3: Top view of printed holder system's bottom section. Copper creep tubes will be placed in the smaller hole section and the sensor would be placed on the larger circle region.

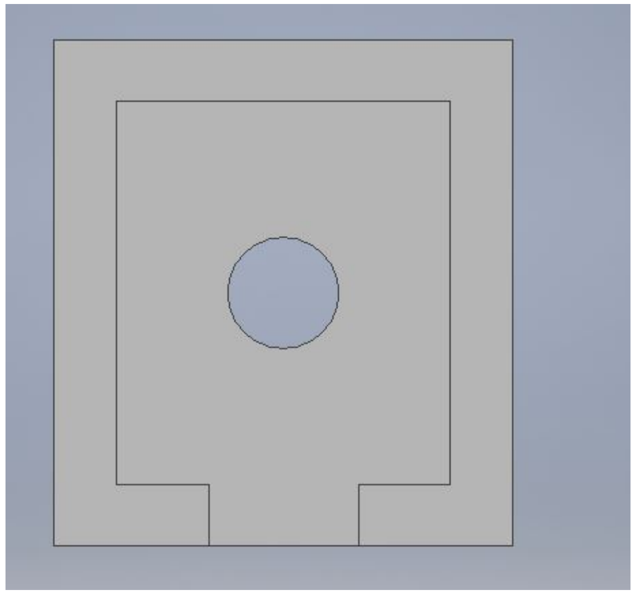

Figure 4.4: Bottom view of printed holder system's top section. This section will be placed over the bottom section. Copper creep tubes will stick out of the top section. An alligator clip is placed on the extended section to provide a grounded signal and keep the rod stable.

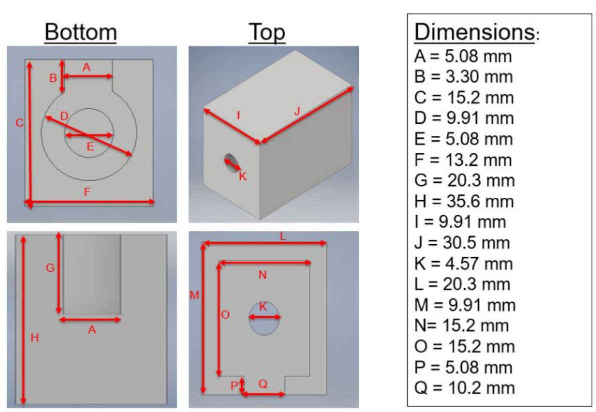

Figure 4.5: Dimensional values of both top and bottom sections of the designed holding device.

Chapter 5

Results

5.1 Simulations

Simulations were performed primarily with constructed finite element method models (FEMM). Two FEMM model versions were created over the course of simulations. Both simulated models include a copper sensor ring, copper creep tube, and PLA holder box. Common items in both models are shown in Figure 5.1. A three dimensional perspective of these models was shown in Figure 3.3. For each simulated model, only the thickness of the copper creep tube changes, all other items are kept constant.

For later simulations all three common components were placed inside of an air box (Figure 3.4). Inclusion of this air box allows for the electromagnetic field to expand out a larger distance, giving a better representation of the real-world system. A larger simulated environment reduces the probability for the electromagnetic field to return to the sensor, lowering the chance of internal coupling in the system. However, the larger this air region, the more computational time and power that must be used when simulating the sensor. To lower the computational time and power, the air box's outer region was placed at a fixed distance from the holder system (forty millimeters). Computational time was also decrease by assuming the model is symmetrical along the z axis (mid plane of the sensor). Our component geometries are simple enough that if the two-dimensional section were rotated around z-axis, then the mean capacitance value would be equal to that of a three-dimensional model.

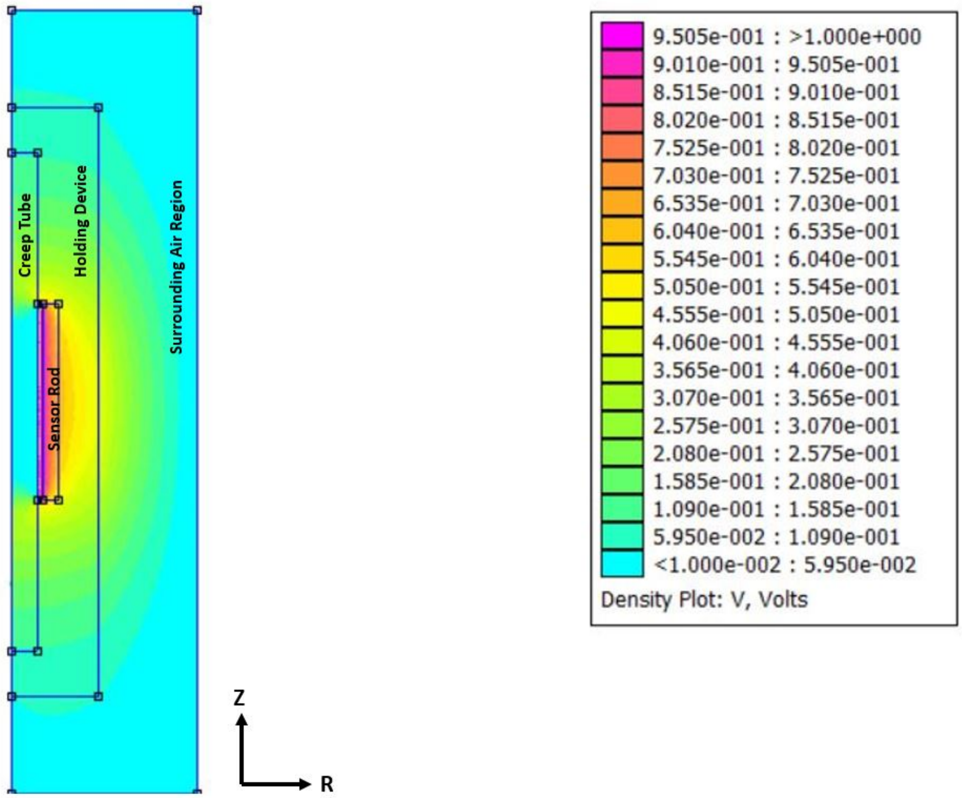

Figure 5.1: Example of earlier developed FEMM model. This model contains only a copper sensor ring, copper tube and PLA holder system. Later models include an air block around the entire system, so as to lower chance of electromagnetic field coupling.

In each simulation the electromagnetic fields are shown with various voltage levels. Voltage level intensity within the simulation samples (Figures 3.4 and 5.1) are shown with a color heat map. Darker colors in the simulations indicate a higher voltage range, with purple being the highest range for the simulation, and lighter colors indicate a lower voltage range, with light blue being the lowest range. Voltage levels indicate the capacitance intensity; this is shown with Faraday's law:

$$I = \frac{V}{R} \tag{5.1}$$

where I is the current signal and R is the resistance in the system. From this equation, the voltage and current signals are proportional to one another. And as mention in previous chapters, the generated current signal is proportional to the capacitance signal. From both simulation versions, the sensor ring has the highest voltage range due to it being declared as the primary component. Primary components are given an initial driving voltage source of 1 volt. Other voltage sources were set as the driving source; however, this value does not impact the simulated capacitance signal. The capacitance signal is influenced by the distance between electrodes, as discussed in previous sections. During simulations, the charge (Q) and voltage (V) signals from the primary source electrons are recorded over the entire simulation process. A mean value for both signal is then used to generate a mean capacitance value (C), ($C = \frac{Q}{V}$). However in earlier simulations, the region to the right of the sensor was shown to have the second highest value range. This is due to the small distance between the sensor and outer holder wall. Because there is no simulated environment behind the holder section, charged particles/polarities are able to "bounce" back from the outer wall to the sensor at an increased rate. As a result of the increase particle movement, the electromagnetic field within that region also increases. However, this increase in electromagnetic field may cause for other regions to experience unrealistic electromagnetic coupling noise. To lower the possibility of internal coupling, the air region was added to later models (Figure 3.4). With this additional region, the electrons have a smaller chance of coming back to the sensor region, thus causing for lower probability of electromagnetic coupling on outer systems. In addition, the extra layer gives the simulation a better representation of the real-world experiment.

Reduction in coupling effects can be well seen in Figure 5.2 where the electromagnetic field decreases in strength as it gets farther from the sensor rod (primary component). This reduction in coupling noise can be seen in the difference in rounded electromagnetic edges. Previous simulation's electromagnetic field shows edges that extend outward. This extension is due to particles scattering off of the holder wall. However, in the newer simulations these fields instead curve inward, indicating that fewer particles are being scattered back. However, this increase in distance does not entirely remove the coupling effects, because the particles still have a chance to scatter off the holder system layer and back to the sensor rod.

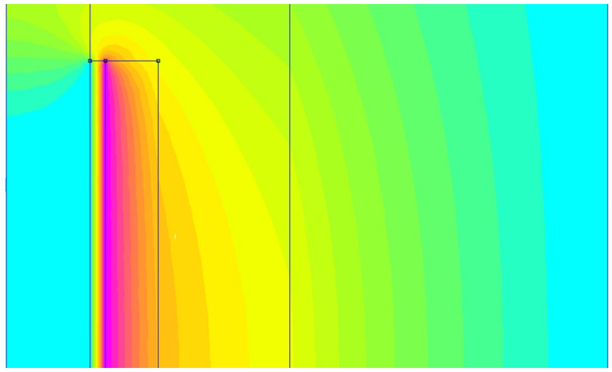

Figure 5.2: Zoomed in section of FEMM models with air block. Inclusion of this section allows for particles to move in a farther direction. Thus reducing the chance of internal coupling effects.

Both FEMM versions were used to simulate the capacitance values for five copper rods with slightly different diameters (4.3942 mm, 4.4069 mm, 4.4196 mm, 4.4323 mm, and 4.445 mm). Simulating rods with such small differences in diameter helps determine if the capacitance values would be differentiable at small intervals and determine if it was possible to measure micron-sized diameter changes. Capacitance values for these rods, from both model versions, are given in Table 5.1.

Table 5.1: Capacitance value comparison of both FEMM model versions

Rod Diameter(mm)	Old FEMM (pF)	Current FEMM (pf)
4.3942	3.6865	4.6446
4.4069	3.7128	4.6729
4.4196	3.7410	4.6998
4.4323	3.7689	4.7266
4.4450	3.7987	4.7573

From Table 5.1, both model versions predict an increasing capacitance trend as the rods swell, indicating that the simulated models do follow the expected distance trend wherein capacitance increases with decreasing electrode distance. The simulated capacitance trends from the earlier version does indicate some coupling effects. Coupling within the simulated models causes for the higher voltage ranges to have more weight on the mean voltage value, causing for the mean capacitance equation ($C = \frac{Q}{V}$) to be heavily influenced by the larger voltage denominator. Due to the increase space in the newer FEMM models, the mean voltage value is less influenced by the higher voltage ranges, and thus gives a higher capacitance value.

5.2 Benchscale Measurements

Following the simulated FEMM models, several real-world systems were constructed to run capacitance tests on various creep tubes. These tests were done by connecting signals to the sensor and creep tube from an AD7747 evaluation board. A 3.3 volt signal was sent to the sensor to generate an electromagnetic field onto it, and the creep tube was kept grounded. Originally in connecting the two wires, a solder connection was utilized. However, this connection proved to be a poor and when placed in the holder unit, the connection would cause for the sensor to pivot towards the creep tube. This pivoting caused for the capacitance signal to go above the evaluation board's upper limit (8.18 pF). To allow for a better connection, a threaded hole was placed on the top of the sensor ring. A single SMB wire is then placed in the hole and kept in place with a micro screw. Such a connection allowed for the SMB wire to have a more direct connection without placing unnecessary material onto the system. In an attempt to keep the creep tube stationary, an alligator clip was connected to the top tube portion during testing.

Similar to the two FEMM models, copper creep tubes with slightly different diameters were tested. This involved testing two step size increments in the creep tubes: 0.127mm (five rods) and 0.0254 mm (seven rods). The 0.127mm creep tube increments were recorded with a sampling rate of 8.1 HZ for nearly one hour each. This low frequency places a larger influence on the resistance leakage terms, causing for the signal to experience a significant drift. Capacitance drift make it hard to distinguish if a creep tube has swelled on not, better seen in Figure 5.3. In addition to internal leakage terms, the system was improperly shielded against external electromagnetic fields and other noise sources, resulting in non-repeatable signals for these constant diameter specimens, shown in Figure 5.4 .

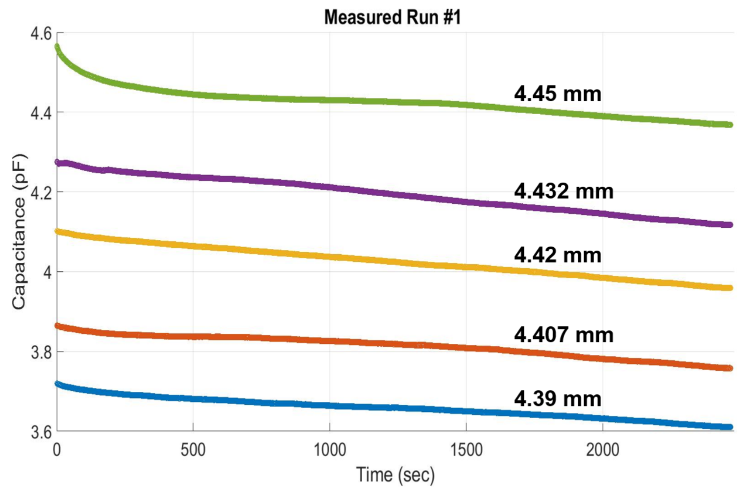

Figure 5.3: Capacitance signals of various non centered creep tubes. Drift in the system makes it harder to differentiate between rods at different time intervals. Samples are taken with an 8.1 HZ sampling rate.

In an attempt to lower the influence from these factors, the recording frequency was increased to 45.5 Hz, with signals being recorded for nearly 66 minutes. An increase in recording frequency lowers the potential for resistor leakage terms to affect the samples. Additionally, an aluminum enclosure was placed around the evaluation board to shield the system. This enclosure reduces the chance of external magnetic fields interacting and potentially coupling with the board; the additional metal layer blocks external electromagnetic fields, allowing for the internal field to have a direct path between charged and grounded layers, as shown in Figure 5.5.

From these new additions, the capacitance signal was measured for seven copper creep tubes with a increasing diameter increments of 0.0254 mm (5.08 mm , 5.11 mm, 5.13 mm, 5.16 mm. 5.18mm 5.21 mm , and 5.23 mm). New diameters were tested to determine if the experimental setup was able to differentiate and record theoretically higher capacitance values. In recording these capacitance values, an external motor was either turned on or off. This motor was included to determine if the shield enclosure would help in reducing

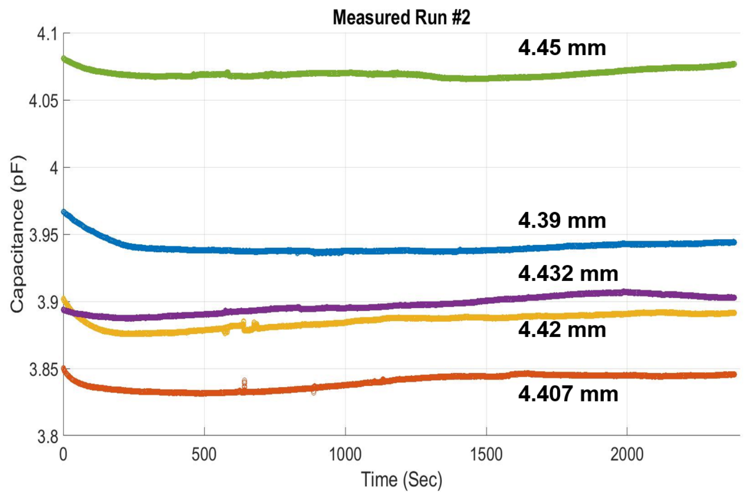

Figure 5.4: Capacitance signals of various non centered creep tubes. These signals were collected post those depicted in Figure 5.3. Drift and external noises cause for non-repeatable and hard to differentiate capacitance signals. Samples are taken with an 8.1 HZ sampling rate.

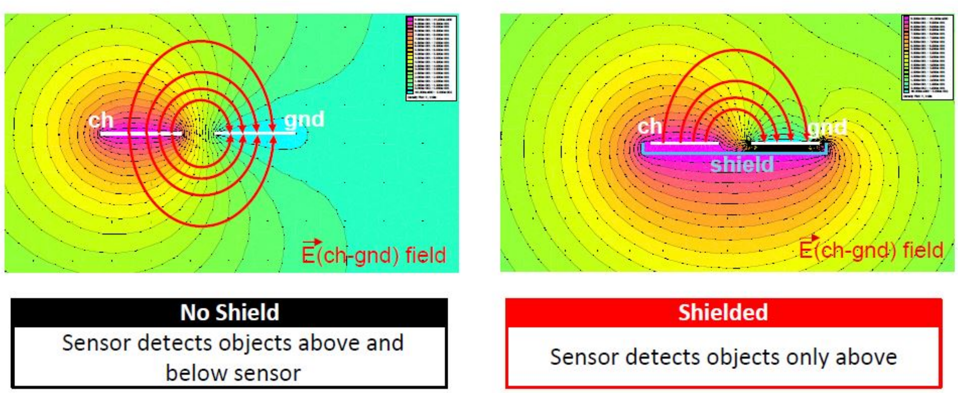

Figure 5.5: Example of electromagnetic field affect on a capacitor with and without an active shield layer. [6]

the noise from external signals. Both Figure 5.6 and 5.7 show that the shield enclosure and higher sampling rate do reduce recorded capacitance drift and overall noise.

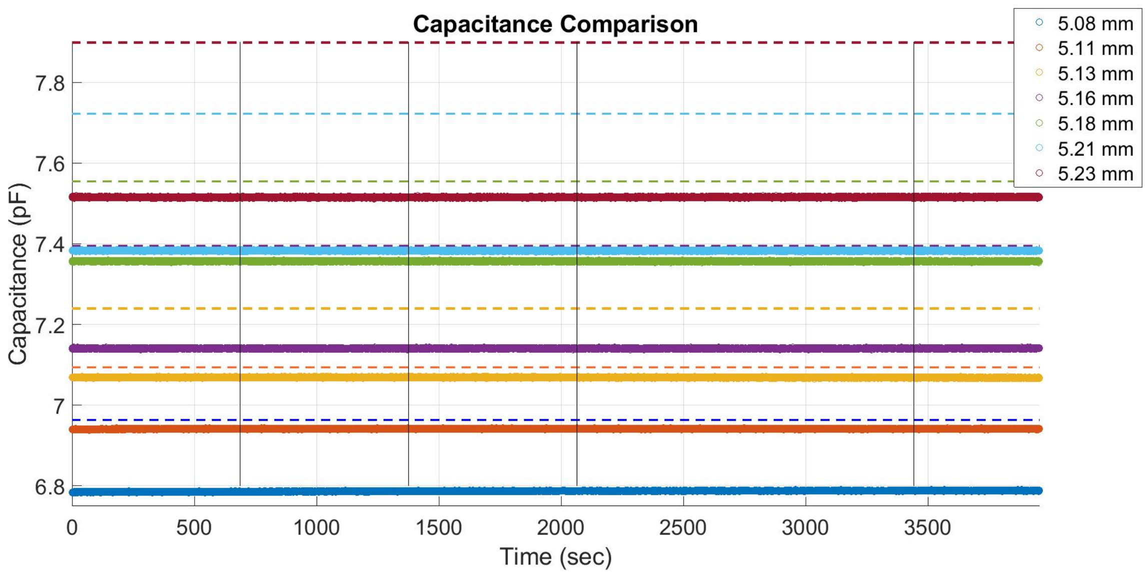

Figure 5.6: Capacitance signals with external motor on. Dashed lines indicate the theoretical capacitance values(pF) of the increasing creep tubes based on Equation 2.6. Samples are taken with an 45.5 HZ sampling rate.

When the motor is operational, the capacitance values for every rod drop by about 0.2 pF, indicating that coupling is still prevalent within the system. This can also be shown by comparing collected values to the theoretical and FEMM values, shown in Table 5.2. Currently, it is assumed that the SMB cable leads to the sensor and creep tube may be experiencing some external coupling, due to their poor shielding. Efforts are in place to replace the cables with a version with a thicker shield (such as a RG316 SMB cable).

Both operational models were then fitted to the cylindrical capacitance trend (Equation 2.6). Fitted models and Figures 5.8 and 5.9, suggest that this approach may be a viable option in monitoring fuel pin diameters. The fitted equations for both models are shown in Equations 5.2 (Machine On) and 5.3 (Machine Off). The y-intercept for both equations is

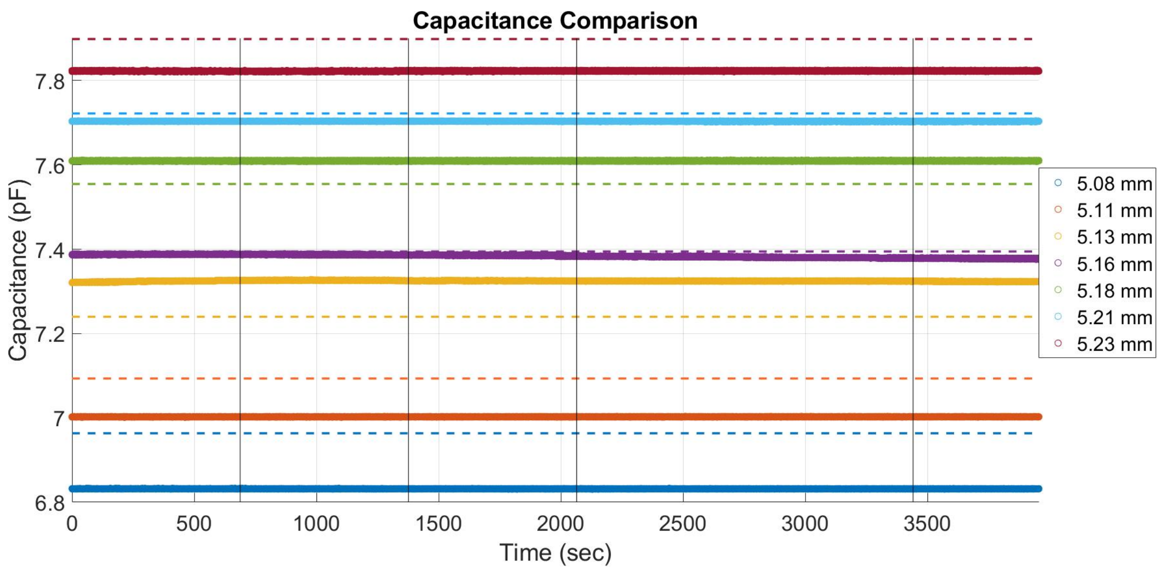

Figure 5.7: Capacitance signals with external motor off. Dashed lines indicate the theoretical capacitance values(pF) of the increasing creep tubes. Samples are taken with an 45.5 HZ sampling rate.

believed to be from noise in the system.

$$y(Machine\,On) = \frac{7.589}{log(\frac{9.017}{x})} - 7.155 \tag{5.2}$$

and

$$y(Machine\,Off) = \frac{10.53}{log(\frac{9.017}{x})} - 12.21. \tag{5.3}$$

where x is the creep tube diameter of interest.

Swelling effects may be monitored following the measurement of the capacitance signal. Regardless of the external machine operation status, the creep tube radius is determined according to:

$$x = \frac{9.017}{e^{\frac{\alpha}{C-\beta}}} \tag{5.4}$$

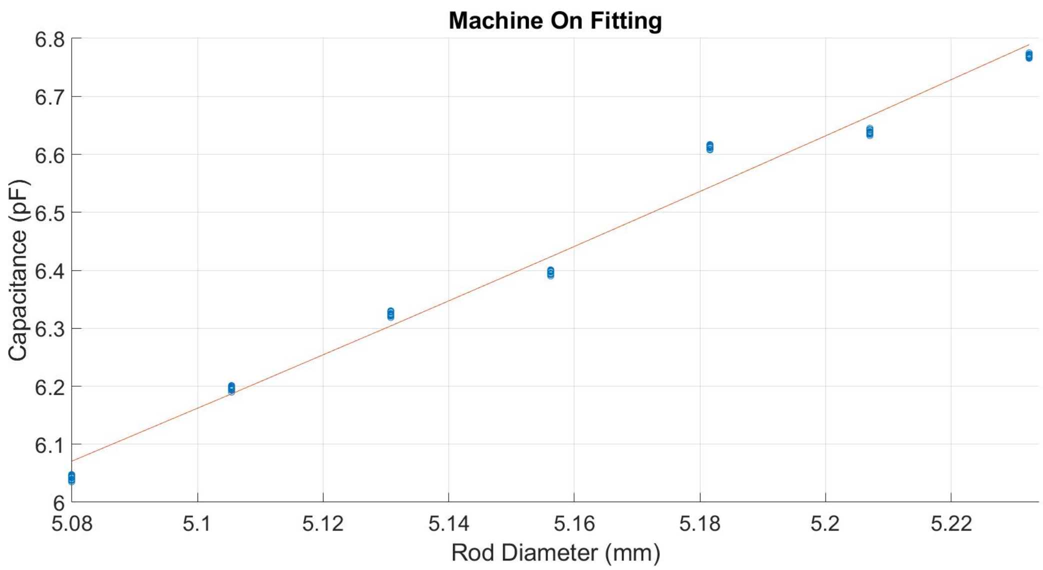

Figure 5.8: Fitting of creep tube diameter to predicted capacitance trend with motor on.

where x is the diameter of the creep tube in mm, C is the measured capacitance in pF, and α and β are the fitted parameters in $y = \frac{\alpha}{log(9.017/x)} + \beta$. Because the test creep tube diameters are fixed, this method may be used to test the accuracy of the sensor. Thus, the internal creep tube diameter calculated from equation 5.4 should be equal to the tested creep tube diameter. However, the collected capacitance signals are exposed to some noise terms. These noise terms create uncertainty in the calculated creep tube dimension.

Table 5.2: Comparison of theoretical mean capacitance values to simulated and real-world models.

Rod Diameter(mm)	Theoretical (pF)	FEMM (pF)	Motor Off (pf)	Motor On (pF)
5.08	6.96	6.96	6.83	6.78
5.11	7.09	7.09	7.00	6.94
5.13	7.22	7.23	7.32	7.07
5.16	7.39	7.39	7.38	7.14
5.18	7.54	7.55	7.61	7.36
5.21	7.72	7.72	7.70	7.38
5.23	7.90	7.90	7.82	7.51

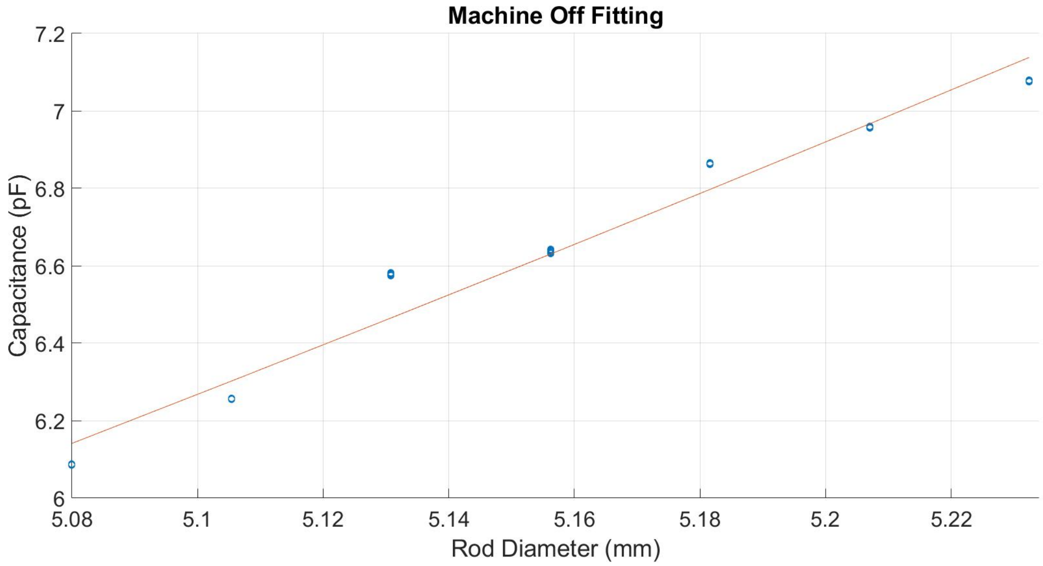

Figure 5.9: Fitting of creep tube diameter to predicted capacitance trend with motor on.

Uncertainty in the diameter values was determined by propagation of uncertainty of equation 5.4. Because the capacitance signal is assumed to be the only term impacted by some noise, the measurement uncertainty in the estimated diameter is:

$$uncertainty = \sqrt{\left(\frac{\alpha * 9.017}{(C-\beta)^2 * e^{\frac{\alpha}{(C-\beta)}}}\right)^2 * (\sigma_C)^2} \tag{5.5}$$

where C is the measured capacitance and σ_C is the standard deviation of the noise in the measured capacitance. For the seven creep tube values, the capacitance standard deviation was:

$$\sigma_C = \sqrt{\frac{\sum_{i=1}^{N}(C_i - \mu_{C,r})^2}{N}} \tag{5.6}$$

where N is the number of capacitance signals, C_i is the measured capacitance signal, and $\mu_{C,r}$ is the mean capacitance signal at radius r. From this method, a higher uncertainty was estimated when the external machine was turned off (average of $\pm 0.22\mu m$) than when the machine was on (average of $\pm 0.16\mu m$). The estimated diameter and uncertainty for the average capacitance measurement for each tube diameter is seen in Figure 5.10.

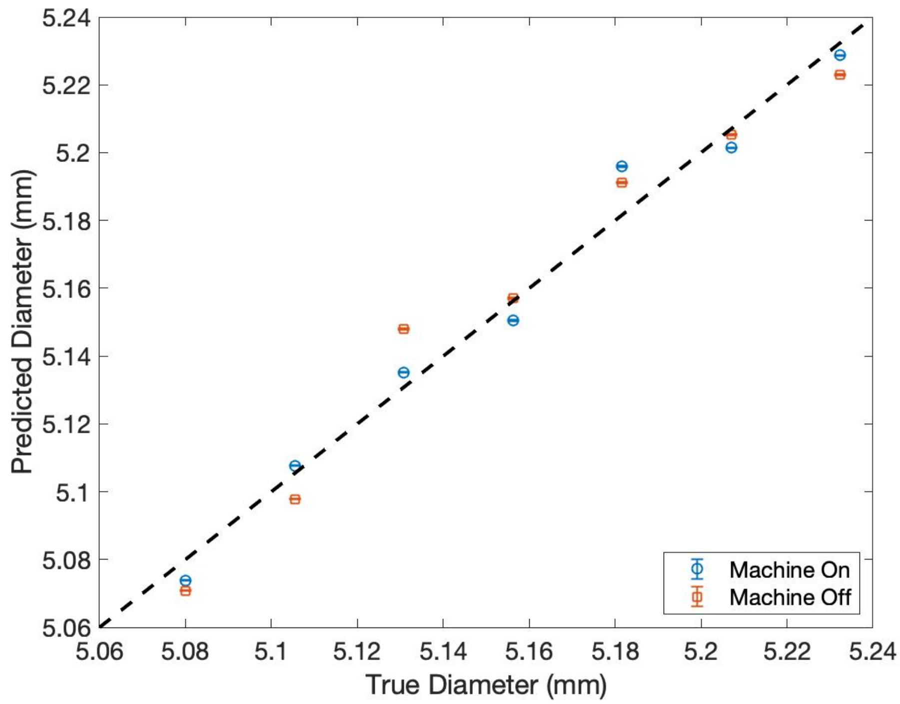

Figure 5.10: Estimation of creep tube diameters from tests with the motor on and off.

The results of this initial bench-scale evaluation of the proposed capacitance-based sensor suggest that this approach can reliably measure small changes in fuel pins. Additional investigation is needed to evaluate the robustness of this sensor to competing effects, like temperature, and the long-term performance in harsh environments.

Chapter 6

Conclusion

Fuel compositions that survive and reliably perform in the harsh environment of reactors for extend periods are vastly need for future reactor's material and *in situ* characteristics. Physics-based simulations of irradiation-, temperature-, pressure-, etc.-induced material degradation, such as creep and swelling, have been used to understand the long-term performance of advanced fuels. As these fuel types are deployed within test reactors and eventually commercial reactors, the measurements and characteristics of the fuel pins can be used to help validate the simulated models. However, current measuring equipment and techniques have a limited operational range due to either the high range of operational temperatures or high power density. Some models also require the use of direct contact, which can cause for inaccurate material characteristic readings. Because of this there is a crucial need for a sensor that can that provide real-time data regarding material evolution under highly accelerated irradiation. A capacitance-based cylindrical sensor has been developed to provide a direct measurement of in-pile dimensional changes due to irradiated fuel swelling.

A cylindrical capacitance displacement sensor was developed for prospective deployment in future fuel irradiation experiments. This has the potential to provide *in situ* data and measurement of the evolution of fuel behavior during irradiation. Prior to development of the model, several simulated models of the sensors were developed. In developing the models two simulators were used: FEMM and EMS. Both simulation methods follow a finite element mesh method, which cuts the entire simulation environment into finite sections/meshes. Equations (e.g. Green's theorem) are solved within each section using values from surrounding regions as inputs. After a section's equations are solved, its values are then sent to neighboring elements. EMS meshes are placed over a three-dimensional environment while the FEMM mesh is over only a simple two-dimensional model. Computational power and time were higher in the EMS simulations because for the three-dimensional volumes. Because of this, FEMM was the primary simulation model. FEMM simulations save computational power and time by simulating only half of a two-dimensional environment. Simulation of half the environment is possible because of the simple shape geometries. And assuming that if these shapes were rotated around the origin then the mean capacitance value would be the same value.

A bench-scale system was created to record the capacitance values from several creep tubes. Two sets of stationary creep tubes were tested, five rods with a step size of 0.127 mm and seven with a 0.0254 mm step size. The small step size increments were chosen to see if the sensor was sensitive enough to differentiate between small diameter changes. Earlier capacitance trends experienced a large drifting trend that made it hard to differentiate between rod capacitance values. Drift in the system was due to resistor leakage from the low sampling frequency (8.1Hz). Additional disturbances were seen from external noise and electromagnetic coupling. System drift was decreased by increasing the sampling rate to 45.5 Hz and placing an aluminum enclosure over the data acquisition board. With these additions in the lab setup, the capacitance values could easily be differentiated between rods sizes. Experimental trends showed that capacitance values increased as the diameter size increase.

From the laboratory and simulated results, the current sensor proves to provide robust and reliable capacitance results. Additional work will be needed to ensure the results remain reliable within a high temperature and irradiated environment. First, the sensor will need to be tested with a medium that is not air. Instead either a gaseous or liquid medium, that more closely represents the fuel rods' surrounding environment, should be used. For a both mediums, the capacitance will need to be tested against various flow rates. Along with the medium alterations, the tested fuel pin should be replaced with material that resemble a test reactor's fuel pin. Doing such provides testing conditions similar to inside a test reactor. Lastly, the testing of temperature effects on the capacitance should be done prior to placement in high gamma and neutron environments. Such testing will help show if the sensor can properly survive the vast operational temperature ranges.

If the further sensor results show to accurately depict fuel rod swelling, then it may be placed within a test reactor whereby *in situ* measurements may be taken from multiple locations on a singular fuel pin, both axially along the height of the fuel pin and radially around the fuel pin. Work by colleagues at INL has investigated the effect of non-concentric electrodes for this type of application. This may be further expanded by introducing non-continuous sensors around the pin diameter to detect local swelling and deformation.

Bibliography

[1] Alenka M. Milovanovic, M. M. B. (2011). Approximate calculation of capacitance of lines with multilayer medium. *Electrical Engineering*, 62(5):249–257. ix, 16, 17

[2] Alessandro Masi, Alessandro Danisi, R. L. M. M. and Spiezia, G. (2011). Study of magnetic interference on an lvdt: Fem modeling and experimental measurements. *Journal of Sensors*. 1

[3] Analog Devices (2008). Eval-ad7747: Evaluation board for 24-bit capacitance-to-digital converter with temperature sensor. http://www.analog.com/media/en/technical-documentation/evaluation-documentation/EVAL-AD7747.pdf. 23

[4] Austin Fleming, Ahmad Al Rashdan, C. J. . P. C. (2019). An impedance-based diameter gauge for in-pile fuel deformation measurements. *Instrumentation Science Technology*, 47:6:611–626. 4

[5] C.S. Chaves, J.R. Camacho, H. P. M. C. and Saraiva, E. (2011). Capacitances calculation using fem for transient overvoltage and common mode currents prediction in inverter-driven induction motors. 18

[6] David Wang (2015). Capacitive sensing:ins and outs of active shielding. Technical Report SNOA926A, Texas instruments. x, 34

[7] Heerens, W. C. (1986a). Application of capacitance techniques in sensor design. *Phys. E: Sci. Instrument*, 19. ix, 8

[8] Heerens, W. C. (1986b). Application of capacitance techniques in sensor design. *Phys. E: Sci. Instrum*, 19(897). ix, 18

[9] Heerens, W.-C. (1986c). Application of capacitance techniques in sensor design. *Journal of physics E: Scientific instruments*, 19(11):897. 14

[10] HoneyWell (2017). Why use linear variable differential transformers. http://www.https://sensing.honeywell.com/aero-lvdt-tech-note_000822.pdf. ix, 12

[11] Hyeong-Joon Ahn, H.-H. K. and Han, D.-C. (2005). Nonlinear analysis of cylindrical capacitive sensor. *Measurement Science and Technology*, 16:699–706. ix, 10, 11

[12] Iskander, M. (2018). Geotechnical underground sensing and monitoring. *Science Direct*. 12

[13] Knol, S., de Koning, A., de Groot, S., Klaassen, F., Bobeldijk, I., Bakker, K., Hania, P., Pouillier, E., and Ambard, A. (2017). Creep measurements on lwr fuel during irradiation. In *2017 Water Reactor Fuel Performance Meeting*, Jeju Island, Korea. ix, 2, 3, 13

[14] Meeker, D. (2014). Finite-element method magnetics: Electrostatics tutorial. 20

[15] Meeker, D. (2018). Finite element method magnetics: User's manual. 20

[16] M.H.W. Bonse, C. Mul, J. S. (1995). Finite-element modelling as a tool for designing capacitive position sensors. *Sensors and Actuators*, A(46-47):266–269. 16

[17] M.H.W Bonse, C. Mul, J. S. (1995). Finite-element modelling as a tool for designing capacitive position sensors. *Sensors and Actuators A*, 46-47:266–269. 20

[18] Puers, R. (1993a). Capacitive sensors: when and how to use them. Sensors and Actuators A:93–105. ix, 9

[19] Puers, R. (1993b). Capacitive sensors: when and how to use them. *Sensors and Actuators A: Physical*, 37:93–105. 4

[20] Queiroz, A. C. M. D. (2012). Capacitance calculations. `http://www.coe.ufrj.br/~acmq/tesla/capcalc.pdf`. 17

[21] R-Wolf, J. (1979). The linear variable differential transformer and its uses for in-core fuel rod behavior measurements. 2

[22] Robert Repas (2007). The hot and cold of lvdts. 13

[23] Uehara, M. (1985). Green's functions and coefficients of capacitance. 19

[24] Xiaohui Hu, W. Y. (2010). Planar capacitive sensors – designs and applications. Sensor Review. 21

[25] Y. Bai, X. Yang, D. Z. X. L. W. C. and Hu, W. (2017). Conducted emi mitigation schemes in isolated switching-mode power supply without the need of a y-capacitor. *IEEE Transactions on Power Electronics*, 432(4):2687–2703. 15

[26] Zhu, F., Spronck, J., and Heerens, W. C. (1991). A simple capacitive displacement sensor. *Sensors and Actuators A: Physical*, 26(1-3):265–269. 4

Vita

Tyler Naughton was born on May 23rd,1996 to John and Jamie Naughton. In May 2018, he received his bachelor's degree in Nuclear Engineering from the University of Tennessee Knoxville. That following fall, he started his master's degree at the same university. During this time frame he presented "CAPACITANCE-BASED DIMENSIONAL CHANGE SENSORS FOR IN-PILE MATERIALS MEASUREMENTS" at the February NPIC-HMIT conference and "Bench-scale Demonstration of a Capacitive Sensor for In-Pile Materials Monitoring" at the winter ANS conference.